ChemComm

COMMUNICATION

View Article Online
View Journal | View Issue

Cite this: *Chem. Commun.*, 2020, **56**, 3963

Received 15th January 2020,
Accepted 28th February 2020

DOI: 10.1039/d0cc00407c

rsc.li/chemcomm

Thiadiazole containing N- and S-rich highly ordered periodic mesoporous organosilica for efficient removal of Hg(II) from polluted water†

Surajit Das,‡[a] Sauvik Chatterjee,‡[a] Saptarsi Mondal,[bc] Arindam Modak,[d] Bijan Krishna Chandra,[ae] Suparna Das,[f] Gilbert Daniel Nessim,[f] Adinath Majee [d] and Asim Bhaumik *[a]

A new N- and S-rich highly ordered periodic mesoporous organosilica material DMTZ-PMO bearing thiadiazole and thiol moieties inside the pore-wall of a 2D-hexagonal nanomaterial has been synthesized. DMTZ-PMO shows a very high surface area (971 $m^2 g^{-1}$), and can be used for efficient and fast removal of Hg^{2+} from polluted water with a very high Hg^{2+} uptake capacity of 2081 mg g^{-1}.

Mercury pollution is a serious threat to mankind as its uptake affects several of our body parts and causes damage in the reproductive, immunity, digestive and central nervous systems.[1] Since the Minemata disaster in Japan,[2] numerous initiatives have been taken to restrict the disposal of mercury[3] and its compounds from industries and combustion of fossil fuels.[4] Thus, continuous research efforts are underway to mitigate mercury's threat and to develop suitable low cost methods for the removal of Hg(II) ions from water resources.[5] In this context, the adsorptive removal of Hg(II) over porous nanomaterials holds great promise due to their high internal surface area, recyclability and greater scope of functional group modification.[6] Although zeolites,[7] activated carbons[8] and clays[9] are intensively studied as Hg(II) adsorbents, they have limited affinity together with moderate uptake capacities. Amine and thiol functionalized porous nanomaterials like metal organic frameworks (MOFs)[10] and covalent organic frameworks (COFs)[11] are used as adsorbents for Hg(II) removal. However, these materials often suffer from serious setbacks due to their instability in the presence of water. Thus, developing functionalized nanomaterials bearing Hg(II) scavenger sites[12] is very demanding as they offer soft–soft interactions with scavenger sites and Hg(II).

Functionalized mesoporous materials with high specific surface area, ordered mesopores and Hg(II) binding sites could be promising adsorbents. Chelating sites bound at the surfaces of SBA-15/MCM-41 could be achieved by anchoring of thiol or amine moieties at the pore surfaces. Periodic mesoporous organosilicas (PMOs)[13] bearing bridging S- and N-rich organic moieties can act as mercury scavengers *via* soft–soft interactions. These PMOs can be synthesized through the co-condensation of bridging organosilanes with tetraalkoxysilanes in the presence of supramolecular assemblies of the surfactant molecules.[13] A large number of bridging organic moieties have been incorporated in the organosilica framework of PMOs[14] to explore their applications in energy, environment and biomedical research. However, the Hg(II) uptake capacities reported over functionalized mesoporous materials and PMOs are quite limited. Recently we have reported a S-rich porous organic polymer SCTN-1 with excellent mercury uptake and fast kinetics.[5c] Hence, in an endeavour to obtain a more robust and economical adsorbent, we herein report a new highly ordered 2D-hexagonal organic–inorganic hybrid mesoporous thiadiazole and thiol functionalized PMO material DMTZ-PMO *via* the substitution reaction of 1,3,4-thiadiazole-2,5-dithiol and 3-choloropropyltriethoxysilane followed by CTAB-assisted hydrothermal synthesis (Scheme 1). The covalently grafted bridging organic functionality inside the mesoporous walls acts as the Hg(II) scavenger and the rigid structure gives stability to the material to act as an excellent adsorbent over a wide range of pH, solvent and temperature. Soft centers, like sulfur, accelerate the mercury ion adsorption through the soft–soft interactions making the material an excellent adsorbent for Hg(II) removal.

Formation of the bridging organosilane (Z) has been confirmed from the ^{1}H NMR spectrum (Fig. S1, ESI†) and FTIR data (Fig. S2, ESI†). PXRD pattern of template-free material (Fig. S3, ESI†) shows strong diffractions for 100, 110, and 200 planes together with a relatively weak diffraction for 210 and 300 planes with peaks at 2θ values of 2.17, 3.77, 4.37, 5.81 and 6.48 revealing a highly ordered 2D-hexagonal mesophase[14b] with the *p6mm* symmetry, having a d_{100} value of 2.017 nm with a lattice constant of a = 2.32 nm.

[a] *School of Materials Sciences, Indian Association for the Cultivation of Science, Jadavpur, Kolkata – 700 032, India. E-mail: msab@iacs.res.in*
[b] *Center for Molecular Spectroscopy and Dynamics, Institute of Basic Science (IBS), Seoul 02841, Republic of Korea*
[c] *Department of Chemistry, Korea University, Seoul 02841, Republic of Korea*
[d] *Department of Chemical Sciences, Ariel University, Ariel-40700, Israel*
[e] *Department of Chemistry Visva-Bharati University, Shantiniketan – 731235, India*
[f] *Department of Chemistry and Bar-Ilan Institute for Technology and Advanced Materials (BINA), Bar-Ilan University, Ramat Gan 5290002, Israel*

† Electronic supplementary information (ESI) available: Detailed synthesis, instrumentation, characterization and NMR data. See DOI: 10.1039/d0cc00407c

‡ These authors have contributed equally.

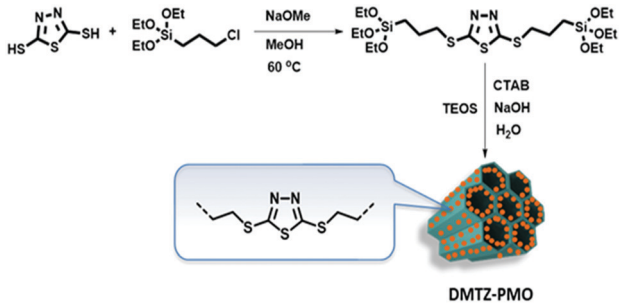

Scheme 1 Synthesis of the organosilane precursor and DMTZ-PMO through the CTAB-assisted supramolecular-templating route.

The presence of the 300 plane indicates a high periodicity of mesopores, which are usually absent in conventional CTAB-templated MCM-41 type materials.[15] Again the PMO material synthesized from pure organosilane precursor Z produces only one diffraction peak corresponding to the disordered mesophase. This result suggested that an optimum (33.33 mol%) amount of TEOS with respect to the total silica content is necessary to promote the cross-linking between the silica moieties and thus to obtain a 2D-hexagonally ordered mesostructure.

The BET surface area and porosity, average pore diameter, and pore volume of the DMTZ-PMO material have been studied from the N_2 adsorption analysis at 77 K. The classical type IV isotherm (Fig. 1a) represents a well-developed mesoporous structure with sharp capillary condensation[15] and a steep N_2 uptake at a lower relative pressure of nitrogen ($P/P_0 < 0.02$). This isotherm revealed a highly porous nanostructure having a BET surface area of 971 $m^2\ g^{-1}$ and an average pore volume of 0.789 cc g^{-1} which decreased to 276 $m^2\ g^{-1}$ and 0.248 cc g^{-1}, respectively, after mercury adsorption from a concentrated Hg(II) solution. The NLDFT model pore size distribution shows two types (1.54 and 2.95 nm) of pores. Bimodal distribution of pores could be attributed to the two sharp increases in the N_2 uptake of the isotherm at $P/P_0 < 0.02$ and 0.3–0.45 regions.

The ^{13}C solid state CP MAS NMR spectrum (Fig. 2) of the as-synthesized DMTZ-PMO material showed strong signals at 14.6, 23.0, 26.2, 30.3, 53.88 and 171.3 ppm for different carbon atoms of the bridging organic moiety. Signals at 129.0, 134.8, and 167.5 reveal that 1,3,4-thiadiazole-2,5-dithiol rich organosilane moieties can exist in three resonance stabilized forms (Fig. 2) providing pseudo aromatic character to the ring.[16] This indicates that the thiol rich organic framework remains intact in the DMTZ-PMO material and becomes an integral part of the mesoporous pore-wall.

The ^{29}Si CP MAS NMR spectrum (Fig. 2) indicates the chemical environment around the silicon atom. The chemical shifts at −79.8 (T^3) and −70.9 (T^2) ppm could be attributed to the $CSi(OSi)_3$ and $CSi(OSi)_2OH$[17] moieties of the PMO framework. A low intensity peak at −61.3 (T^1) ppm could arise due to $CSi(OSi)(OH)_2$.[17a] Another two peaks at −101.0 and −110.6 ppm are due to the Q^3 and Q^4 silica species, which ensure the presence of $Si(OSi)_n(OH)_{4-n}$.[18]

The nanostructure and particle morphology of the material have been visualized from the HRTEM images, (Fig. 1b and c) which confirm the uniform mesopores throughout the whole specimen with a high periodicity of the 2D-hexagonal arrangement of pores having an average pore width of 2.25 nm and a pore wall thickness of 1.25 nm. The electron density elemental mapping analysis over the carbon and sulfur atoms (Fig. S4, ESI†) suggested that sulfur atoms are homogeneously distributed throughout the material. The SEM images (Fig. S5, ESI†) suggested a 150–200 nm size spherical particle morphology for DMTZ-PMO. The FTIR spectrum (Fig. S6, ESI†) of the template free DMTZ-PMO material shows a broad band centered at 3423 cm^{-1}, which is due to the Si–OH bond.[19] A characteristic Si–O–Si stretching band at 1072 cm^{-1},[20] and two bands for >N–C═S and –N═C–S fragments at 1440 and 1501 cm^{-1} appeared, which confirm the existence of thiol rich organic moieties inside the PMO framework. The strong characteristic signal at 715 cm^{-1} could be assigned to the C–S bond stretching.[21]

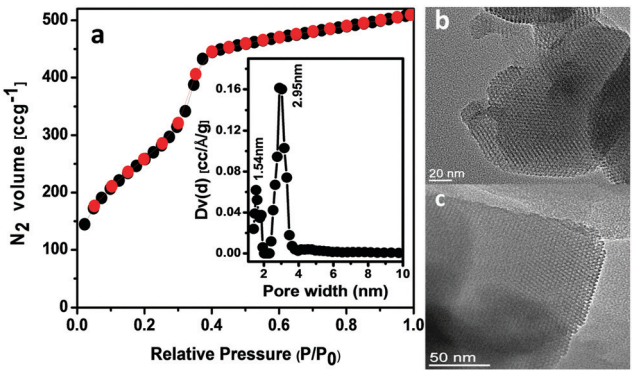

Fig. 1 N_2 adsorption/desorption isotherm of DMTZ-PMO (a). Adsorption points are black circles and those of desorption are red. PSD plot of the material employing the NLDFT model is shown in the inset. HRTEM images of DMTZ-PMO at different magnifications (b and c).

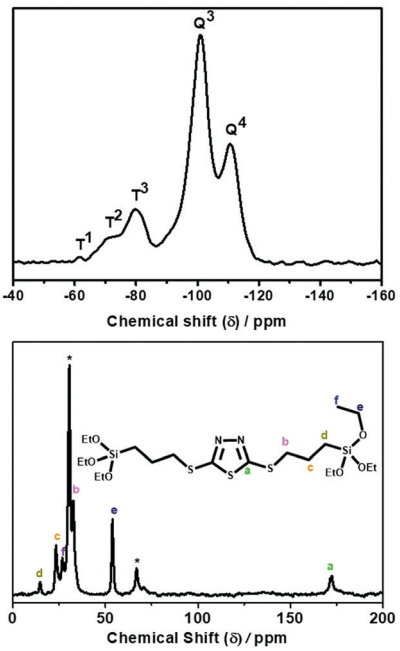

Fig. 2 ^{29}Si MAS NMR Spectra of DMTZ-PMO (up). ^{13}C CP-MAS NMR spectra of DMTZ-PMO (down). * Corresponds to C of CTAB (ESI†).

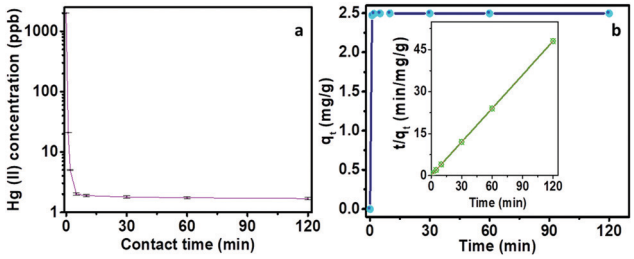

Fig. 3 Mercury adsorption kinetics of DMTZ-PMO with an initial Hg(II) concentration of 2 ppm (a). Hg(II) concentration *vs.* contact time in aqueous solution for 2 ppm solution (b) Pseudo-second-order kinetics for the adsorption with 2 ppm Hg(II) is shown in the inset.

The presence of S atoms as a soft basic centre within the material helps in its Hg(II) uptake capacities from different aqueous solutions. As per the World Health Organization (WHO), safe health drinking water standard permissibility for Hg(II) in drinking water is 2.0 ppb. The ground water Hg(II) content differs upon geographical locations[22] and industrial contamination due to the quantity of mercury waste. Keeping in mind the necessity of fast removal of Hg(II), we carried out the uptake kinetics study over our PMO material and concentrations of mercury at different time intervals (Fig. 3a and b) are estimated by using ICP-OES. Our experimental data revealed that the mercury concentration reduced from 2 ppm to less than 2 ppb as an equilibrium concentration within just 5 min, (Fig. 3a) which is well below the WHO permissible limit. Various adsorption kinetics models were tried to understand the real kinetics of adsorption. The Lagergren first order equation was used for fitting of the data and it was found to be very poor fitting with the residual sum value, *ca.* 34. The pseudo second order kinetics model was tried for the fitting of the concentration data using the Ho and McKay Model with a rate constant of 107 g mg^{-1} min^{-1} (eqn (2.1)).[23]

$$\frac{t}{q_t} = \frac{1}{k_2 q_e^2} + \frac{t}{q_e} \quad (2.1)$$

where k_2 is the adsorption rate constant (g mg^{-1} min^{-1}). q_e and q_t are the Hg^{2+} uptake capacities (mg g^{-1}) at equilibrium and at time t, respectively. The initial adsorption rate, h ($k_2 q_e^2$), is considered as the scale for evolution of the quality of the adsorbent which is numerically 671 mg g^{-1} min^{-1} for our PMO material, indicating a very fast uptake even at low mercury concentration, which outperforms COF-S-SH (143 mg g^{-1} min^{-1}).[24] k_2 for DMTZ-PMO is higher than for most of the benchmark mercury adsorbent materials reported earlier[5] and recently reported materials like TPB-DMTP-COF-SH (11.8 g mg^{-1} min^{-1})[25] and PAF-1-SH (8.13 g mg^{-1} min^{-1}).[26] The distribution coefficient, (K_d), for DMTZ-PMO was analyzed by the following equation (eqn (2.2)).

$$K_d = \frac{(C_0 - C_e)}{C_e} \times \frac{V}{m} \quad (2.2)$$

here, m denotes the amount of the adsorbent material taken (g), C_0 and C_e are the initial and equilibrium concentrations of Hg^{+2}, and V is the volume of the solution taken. The mercury removal efficiency was found to be 99.9% in 5 min. The distribution coefficient (K_d) for Hg(II) uptake upon DMTZ-PMO was 2.5×10^6 mL g^{-1}, which is well above that of other well-known adsorbents (1.0×10^5 mL g^{-1})[27] together with the retention of adsorption capacity in a wide pH range of 1–8. Fast uptake with an excellent Hg(II) adsorption capacity of 2081 mg g^{-1} for DMTZ-PMO is comparable to those of the benchmark mercury adsorbents and the state of art functionalized nanomaterials.[28] This material also showed very high recyclability for several adsorption cycles with a removal efficiency of 99.9% at the 6th cycle (Fig. S7, ESI†). The small angle XRD and HRTEM images of DMTZ-PMO after 6 adsorption cycles confirmed the retention of 2D-hexagonal mesophases (Fig. S8 and S9, ESI†). In nature, mercury is often found in the form of organomercury sources. Thus, we have studied the methylmercury(II) uptake by DMTZ-PMO. 200 ppb methylmercury(II) iodide showed 73.3% removal efficiency within 5 min and the highest uptake capacity of 268 mg g^{-1} at pH *ca.* 6.5, which is much larger than the previous reports.[12h] The lower adsorption capacity for methylmercury(II) over Hg(II) can be attributed to the lower binding affinity of CH_3Hg^+ than Hg^{2+}.[12h] Mercury vapor from the mining industry and soil[29] is another source of mercury pollution. DMTZ-PMO showed a Hg vapor adsorption of 378 mg g^{-1} at 150 °C, which is much higher than that of the activated carbon (47 mg g^{-1}).[5c] Due to the soft–soft interaction, this adsorbent can capture ions like Cd^{2+}/Pb^{2+}, but the uptake of Na^+ or K^+ is negligible (Fig. S10, ESI†). However, the presence of other metal cations does not interfere in the adsorption performance for Hg(II) over DMTZ-PMO. The XPS analysis of the DMTZ-PMO sample after Hg^{2+} adsorption has been carried out to understand the nature of Hg–S binding. It was observed that the S2p peak shifts from 163.0 to 163.6 eV, indicating the bonding interaction between the S center of the material and Hg (Fig. S11, ESI†).[5c] The Hg4s peak seen at 803.7 eV indicates the presence of adsorbed Hg in DMTZ-PMO.

We have performed the *ab initio* quantum chemical calculations for the complexes (Hg^{2+}:DMTZ-PMO) by varying the molar ratios of repetitive units of the PMO (Z, bridging organic group) with Hg(II) to understand the adsorption mechanism. Fig. S12a–d (ESI†) show only the most stable conformer for the 1 : 1 complex, A1 Fig. S12(a) and 2 : 1 conformer B1 Fig. S12(b) (ESI†). All the optimized geometries from mono- to tri-mercuric complexes (A1–A5, B1–B6, and C1–C2) are shown in Fig. S13 (ESI†). The stabilization energy and the non-covalent distances for the most stable conformers (Table S1, ESI†) revealed A1 with a stabilization energy of 204.7 kcal mol^{-1}, where Hg^{2+} binds with O, N, S and H–C groups of the thiadiazole and thiol moieties through $Hg^{2+}\cdots O$, $Hg^{2+}\cdots N$, $Hg^{2+}\cdots S$, and $Hg^{2+}\cdots H$–C interactions with the respective interactive distances of 2.23, 2.25, 2.86, and 2.74 Å. The stabilization energy for the dimercuric B1 complex is 166.8 kcal mol^{-1}, having one end $Hg^{2+}\cdots O$, $Hg^{2+}\cdots O$, and other end $Hg^{2+}\cdots N$, $Hg^{2+}\cdots S$, $Hg^{2+}\cdots H$–C interactions with the respective interactive distances of 2.30, 2.30, and 2.38, 2.69, 2.61 Å, respectively (Fig. 4).

The nature and strength of these non-covalent interactions are examined using AIM analysis and the generated molecular density map (Table S2 and Fig. S14, ESI†). In A1, the ρ and $\nabla^2\rho$ values for the $Hg^{2+}\cdots O$ interactions are 0.067, and 0.282; that for $Hg^{2+}\cdots N$ are 0.075, and 0.236; for $Hg^{2+}\cdots S$ are 0.035, and 0.086; and for $Hg^{2+}\cdots H$–C interactions are 0.011, and 0.039 a.u., respectively. In B1, Hg^{2+} binds with the O atom cyclically in the one end of the ligand with ρ and $\nabla^2\rho$ values around 0.058 and, 0.238 a.u.,

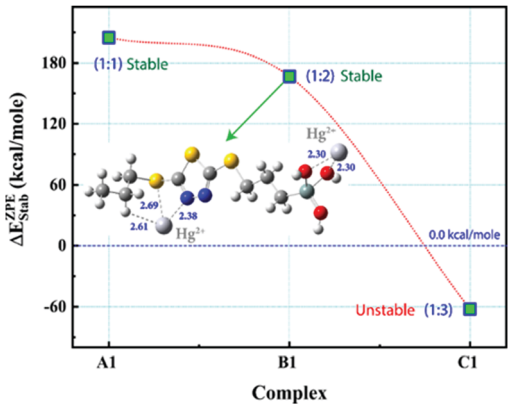

Fig. 4 Stabilization energy plot of the complex between Hg^{2+} and the ligand concerning the number of Hg^{2+} ions. The spheres indicate white = H, yellow = S, grey = C, light blue = Si, blue = N, red = O and light grey = Hg.

respectively. The other end ρ and $\nabla^2\rho$ values for $Hg^{2+}\cdots N$ interactions are 0.056 and 0.188 a.u., and that for $Hg^{2+}\cdots S$ are 0.049 and 0.098 a.u., and for $Hg^{2+}\cdots H$–C are 0.015 and 0.045 a.u. respectively. For all (A1–A5, B1–B6) complexes the values of topological parameters are well above the criteria for consideration of non-covalent interactions and these further reveal that $Hg^{2+}\cdots O$, and $Hg^{2+}\cdots N$ are very strong, $Hg^{2+}\cdots S$ is moderately strong, and $Hg^{2+}\cdots H$–C is very weak non-covalent interactions, suggesting profound sigma bond characters (Table S2, ESI†).

N- and S-rich highly ordered 2D-hexagonal PMO materials bearing 1,3,4-thiadiazole-2,5-dithiol moieties can be synthesized through the surfactant assisted method. Due to its high surface area and strong binding affinity this PMO displayed a very fast and exceptionally high Hg(II) uptake (2081 mg g^{-1}) suggesting it as a prolific adsorbent for sustainable and clean water supply in future.

SD would like to thank the CSIR, New Delhi, for his senior research fellowship. SC wishes to thank DST, New Delhi, for a senior research fellowship. AB would like to thank DST-SERB for a research grant.

Conflicts of interest

The authors declare no competing financial interest.

Notes and references

1 (*a*) T. W. Clarkson, *Environ. Health Perspect.*, 1992, **100**, 31–38; (*b*) L. J. Esdaile and J. M. Chalker, *Chem. – Eur. J.*, 2018, **24**, 6905–6916.
2 M. Harada, *Crit. Rev. Toxicol.*, 1995, **25**, 1–24.
3 S. Engels, L. S. R. Z. Fong, Q. Chen, M. J. Leng, S. McGowan, M. Idris, N. L. Rose, M. S. Ruslan, D. Taylor and H. Yang, *Environ. Pollut.*, 2018, **235**, 907–917.
4 E. G. Pacyna, J. M. Pacyna, F. Steenhuisen and S. Wilson, *Atmos. Environ.*, 2006, **40**, 4048–4063.
5 (*a*) B. Li, Y. Zhang, D. Ma, Z. Shi and S. Ma, *Nat. Commun.*, 2014, **5**, 5537; (*b*) D. Esquivel, J. Ouwehand, M. Meledina, S. Turner, G. Van Tendeloo, F. L. Romero-Salguero, J. De Clercq and P. Van Der Voort, *J. Hazard. Mater.*, 2017, **339**, 368–377; (*c*) S. Mondal, S. Chatterjee, S. Mondal and A. Bhaumik, *ACS Sustainable Chem. Eng.*, 2019, **7**, 7353–7361.
6 (*a*) L. Meri-Bofi, S. Royuela, F. Zamora, M. L. Ruiz-González, J. L. Segura, R. Muñoz-Olivas and M. J. Mancheño, *J. Mater. Chem. A*, 2017, **5**, 17973; (*b*) M. Mureseanu, A. Reiss, N. Cioatera, I. Trandafir and V. Hulea, *J. Hazard. Mater.*, 2010, **182**, 197–203; (*c*) D. Shetty, S. Boutros, A. Eskhan, A. M. De Lena, T. Skorjanc, Z. Asfari, H. Traboulsi, J. Mazher, J. Raya, F. Banat and A. Trabolsi, *ACS Appl. Mater. Interfaces*, 2019, **11**, 12898–12903.
7 H. Javadian and M. Taghavi, *Appl. Surf. Sci.*, 2014, **289**, 487–494.
8 A. K. Meena, G. K. Mishra, P. K. Rai, C. Rajagopal and P. N. Nagar, *J. Hazard. Mater.*, 2005, **122**, 161–170.
9 R. Celis, M. C. Hermosin and J. Cornejo, *Environ. Sci. Technol.*, 2000, **34**, 4593–4599.
10 (*a*) L. Ding, X. B. Luo, P. H. Shao, J. K. Yang and D. Q. Sung, *ACS Sustainable Chem. Eng.*, 2018, **6**, 8494–8502; (*b*) P. F. Yang, Y. F. Shu, Q. X. Zhuang, Y. S. Li and J. L. Gu, *Chem. Commun.*, 2019, **55**, 12972–12975; (*c*) D. T. Sun, L. Peng, W. S. Reeder, S. M. Moosavi, D. Tiana, D. K. Britt, E. Oveisi and W. L. Queen, *ACS Cent. Sci.*, 2018, **4**, 349–356.
11 Q. Sun, B. Agulia, J. Perman, L. D. Earl, C. W. Abney, Y. C. Cheng, H. Wei, N. Nguyen, L. Wojtas and S. Q. Ma, *J. Am. Chem. Soc.*, 2017, **139**, 2786–2793.
12 (*a*) V. Antochshuk and M. Jaroniec, *Chem. Commun.*, 2002, 258–259; (*b*) V. Antochshuk, O. Olkhovyk, M. Jaroniec, I. S. Park and R. Ryoo, *Langmuir*, 2003, **19**, 3031–3034; (*c*) D. Pérez-Quintanilla, I. del Hierro, M. Fajardo and I. Sierra, *J. Environ. Monit.*, 2006, **8**, 214–222; (*d*) D. Pérez-Quintanilla, I. del Hierro, M. Fajardo and I. Sierra, *J. Hazard. Mater.*, 2006, **B134**, 245–256; (*e*) Q. Li, Z. Wang, D. M. Fang, H.-Y. Qu, Y. Zhu, H.-J. Zou, Y.-R. Chen, Y.-P. Du and H. L. Hu, *New J. Chem.*, 2014, **38**, 248–254; (*f*) R. Gomes and A. Bhaumik, *Microporous Mesoporous Mater.*, 2015, **207**, 71–77; (*g*) S. L. Pan, K. Li, L. L. Li, M. Y. Li, L. Shi, Y. H. Liu and X. Q. Yu, *Chem. Commun.*, 2018, **54**, 4955–4958; (*h*) S. Xia, Y. Huang, J. Tang and L. Wang, *Environ. Sci. Pollut. Res.*, 2019, **26**, 8709–8720.
13 S. Inagaki, S. Guan, Y. Fukushima, T. Ohsuna and O. Terasaki, *J. Am. Chem. Soc.*, 1999, **121**, 9611–9614.
14 (*a*) D. Chandra, T. Yokoi, T. Tatsumi and A. Bhaumik, *Chem. Mater.*, 2007, **19**, 5347–5354; (*b*) E. B. Cho, D. Kim, J. Górka and M. Jaroniec, *J. Mater. Chem.*, 2009, **19**, 2076–2081; (*c*) G. Ekineker, C. Nguyen, S. Bayir, G. S. Dominguez, U. Isci, M. Daurat, A. Godefroy, L. Raehm, C. Charnay, E. Oliviero, V. Ahsen, M. Gary-Bobo, J. O. Durand and F. Dumoulin, *Chem. Commun.*, 2019, **55**, 11619–11622.
15 C. T. Kresge, M. E. Leonowicz, W. J. Roth, J. C. Vartuli and J. S. Beck, *Nature*, 1992, **359**, 710–712.
16 G. D. Thorn, *Can. J. Chem.*, 1960, **38**, 139–1444.
17 (*a*) M. Masakatsu Kuroki, T. Asefa, W. Whitnal, M. Kruk, C. Yoshina-Ishii, M. Jaroniec and G. A. Ozin, *J. Am. Chem. Soc.*, 2002, **124**, 13886–13895; (*b*) A. Modak, A. K. Barui, C. R. Patra and A. Bhaumik, *Chem. Commun.*, 2013, **49**, 7644–7646.
18 R. Kumar, A. Bhaumik, R. K. Ahedi and S. Ganapathy, *Nature*, 1996, **381**, 298–300.
19 T. M. Albayati, G. M. Alwan and O. S. Mehdy, *Korean J. Chem. Eng.*, 2017, **34**, 259–265.
20 F. Raji and M. Pakizeh, *Appl. Surf. Sci.*, 2013, **282**, 415–424.
21 W. Guo, K. L. Tao, W. Tan, M. M. Zhao, L. Y. Zheng and X. L. Fan, *Org. Chem. Front.*, 2019, **6**, 2048–2066.
22 R. P. Schwarzenbach, B. I. Escher, K. Fenner, T. B. Hofstetter, C. A. Johnson, U. Von Gunten and B. Wehrli, *Science*, 2016, **313**, 1072–1077.
23 Y. S. Ho and G. Mckay, *Process Biochem.*, 1999, **34**, 451–465.
24 Q. Sun, B. Aguila, J. Perman, L. D. Earl, C. W. Abney, Y. Cheng, H. Wei, N. Nguyen, L. Wojtas and S. Q. Ma, *J. Am. Chem. Soc.*, 2017, **139**, 2786–2793.
25 L. Merí-Bofí, S. Royuela, F. Zamora, M. L. Ruiz-González, J. L. Segura, R. Muñoz-Olivas and M. J. Mancheño, *J. Mater. Chem. A*, 2017, **5**, 17973–17981.
26 B. Li, Y. Zhang, D. Ma, Z. Shi and S. Ma, *Nat. Commun.*, 2014, **5**, 5537.
27 Y. S. Shin, G. E. Fryxell, W. Um, K. Parker, S. V. Mattigod and R. Skaggs, *Adv. Funct. Mater.*, 2007, **17**, 2897–2901.
28 (*a*) L. Zhang, W. Zhang, J. Shi, Z. Hua, Y. Li and J. Yan, *Chem. Commun.*, 2003, 210–211; (*b*) P. Figueira, M. A. O. Lourenço, E. Pereira, J. R. B. Gomes, P. Ferreira and C. B. Lopes, *J. Environ. Chem. Eng.*, 2017, **5**, 5043–5053.
29 (*a*) Global Mercury assessment, UN Environment, 2018; (*b*) M. J. H. Worthington, *et al.*, *Chem. – Eur. J.*, 2017, **23**, 16219–16230.

